Dalton Transactions

PAPER

View Article Online
View Journal | View Issue

Published on 25 June 2018. Downloaded by University of Tennessee at Knoxville on 9/5/2018 8:48:37 PM.

Check for updates

Cite this: *Dalton Trans.*, 2018, **47**, 9765

Synthesis, characterization and photocatalytic activity of mixed-metal oxides derived from NiCoFe ternary layered double hydroxides

Duo Pan,[a] Shengsong Ge,*[a] Junkai Zhao,[a,d] Qian Shao,[a] Lin Guo,[a] Xincheng Zhang,[a] Jing Lin,*[b] Gaofeng Xu*[c] and Zhanhu Guo *[d]

Ternary NiCoFe mixed-metal oxides (NCF-MMOs) with different Ni/Co/Fe ratios were successfully synthesized through a hydrotalcite-like precursor route by co-precipitation of appropriate amounts of metal salts from homogeneous solution, followed by calcination at 600 °C. X-ray diffraction (XRD) patterns revealed the formation of well crystalline layered double hydroxides (LDHs), particularly at the M^{2+}/M^{3+} ratio of 3 : 1. Brunauer–Emmett–Teller (BET) analysis revealed that the resulting NiCoFe LDHs possessed large specific surface areas (66.9–93.8 $m^2\ g^{-1}$). The NCF-MMO (1 : 2 : 1) samples were demonstrated to be formed by the aggregation of regular cubes with an edge length of about 2 μm, and each cube was accumulated with many fine particles with a size of ~130 nm. UV–vis diffuse reflection spectroscopy (DRS) confirmed that the samples showed a broad absorption in the visible-light region (450–750 nm), with a low band gap of 2.33–2.77 eV. The calcined samples with a Ni/Co/Fe molar ratio of 1 : 2 : 1 possessed the best photocatalytic activity with 96.8% degradation of methylene blue (MB) dye under visible light irradiation for 4 h, which exceeded those of commercial P25 TiO_2, binary NiFe mixed-metal oxides and pure Fe_2O_3, CoO and NiO particles under the same conditions. NCF-MMO (1 : 2 : 1) also had a strong degradation effect on the non-dye pollutant phenol as well. Kinetic studies suggested that the degradation of MB followed a pseudo-first-order kinetic behavior. The photodegradation mechanism of NCF-MMOs was also discussed.

Received 19th March 2018,
Accepted 25th June 2018

DOI: 10.1039/c8dt01045e

rsc.li/dalton

1. Introduction

Industrial waste water has become one of the main environmental concerns because it contains a wide range of harmful organic compounds and toxic substances.[1–4] The efficient removal of organic dyestuffs in industrial polluted water has always been a hot and challenging issue in the field of environmental remediation and pollution control.[5–8] There are several methods reported to remove organic compounds from water: flocculation, adsorption and microbial degradation; however, these traditional methods proved to be not very efficient.[9–14]

Photocatalysis using semiconductors has been extensively investigated for the removal of organic dyestuffs thanks to the rapid development of nanostructured oxide semiconductors, which can efficiently utilize UV and abundant solar light as a driving energy source.[15–17] In particular, the photocatalytic degradation of organic pollutants and dyes under visible light has gained momentum over the past decade as a platform for the development of novel synthetic transformations *via* the implementation of non-traditional degradation mechanisms.[18] Many materials including TiO_2 and ZnO have attracted great interest as promising photocatalysts in the fields of environmental pollution control and solar energy conversion, due to their high photocatalytic activity, low cost, resistance to photocorrosion, photo-stability and non-toxicity.[19,20] For example, Yang *et al.* synthesized TiO_2 microtubes *via* a simple and efficient double soaking sol–gel route and evidenced that the materials showed a good photocatalytic performance under UV irradiation.[21]

However, both TiO_2 and ZnO exhibit low quantum efficiencies which limit their effectiveness under visible light illumination because they are usually activated under UV-light

[a]*College of Chemical and Environmental Engineering, Shandong University of Science and Technology, Qingdao 266590, PR China. E-mail: shengsge@gmail.com*
[b]*School of Chemistry and Chemical Engineering, Guangzhou University, Guangzhou 510006, P.R. China. E-mail: linjing@gzhu.edu.cn*
[c]*College of Chemical Engineering, Southwest Forestry University, Kunming 650224, China. E-mail: xgf0208@163.com*
[d]*Integrated Composites Laboratory (ICL), Department of Chemical & Biomolecular Engineering, University of Tennessee, Knoxville, TN 37996, USA. E-mail: zguo10@utk.edu*

Published on 25 June 2018. Downloaded by University of Tennessee at Knoxville on 9/5/2018 8:48:37 PM.

irradiation due to their large band gaps.[22–24] Therefore, it is extremely important to develop a stable and easily-made oxide photocatalyst that can harness visible light with high efficiency under normal sunlight conditions. Thus, composite metal oxides composed of ion doping and metal doping have attracted much attention for the purpose of introducing energy levels in the band gap.[25,26] For example, Rawool *et al.* successfully doped nickel into TiO_2 to obtain NiTi composites. The composite of p–n oxides offered a lower band gap energy of 2.67 eV as compared to both pure oxides TiO_2 and NiO with effectiveness in charge separation across the p–n junction, leading to an efficiently improved photocatalyst.[27]

Mixed metal oxides (MMOs) prepared by the thermal treatment of layered double hydroxides (LDHs) have been applied as catalysts,[28] adsorbents,[29] anion exchangers[30] and so on. The generalized chemical formula of LDHs is: $[M^{2+}_{(1-x)}M^{3+}_{x}(OH)_2]^{x+}[A^{n-}_{x/n}]\cdot mH_2O$, where M^{2+} and M^{3+} represent divalent (Mg^{2+}, Zn^{2+}, Co^{2+}, Cu^{2+}, Ni^{2+}, Mn^{2+}, *etc.*) and trivalent (Al^{3+}, Fe^{3+}, Cr^{3+}, Ga^{3+}, V^{3+}, Ti^{3+}, *etc.*) metal cations, respectively; A^{n-} stands for the interlayer anions (NO_3^-, Cl^-, OH^-, CO_3^{2-}, SO_4^{2-}, *etc.*).[31–33] The LDHs synonymous with naturally occurring hydrotalcite-like phases might provide great potential for their applications in dye degradation because of their special and manageable structure with a very wide range of chemical compositions and different metals and proportions in LDHs.[34,35] Furthermore, the calcination of LDH materials at moderate temperature (300–600 °C) leads to the formation of highly active MMO nanocomposites with a high specific surface area and thermal stability,[36,37] which can tune the semiconductor properties of the MMO materials and facilitate the transfer of the photogenerated electrons to the surface of photocatalysts.[38] Starukh *et al.* recently conducted studies on the thermal treatment of ZnAl-LDH at 400 °C with different Zn^{2+}/Al^{3+} molar ratios, which showed an enhanced photocatalytic activity with increasing molar ratio.[39] Silva *et al.* synthesized ZnCr-LDH *via* the simple coprecipitation method and evidenced that the materials showed a high photocatalytic performance.[40] Although binary MMO materials as photocatalysts have been thoroughly studied, ternary and multicomponent LDHs in photocatalysis have rarely been investigated; in particular, there is almost no report for metals such as Ni, Co and Fe to serve as LDH precursors. It is of great significance to efficiently utilize Earth-abundant metal elements (*e.g.* Ni and Fe) for the synthesis of high performance photocatalysts.

In this work, we synthesized a series of NiCoFe MMOs (NCF-MMOs) using the co-precipitation method. The photocatalytic performance was tested by measuring the degradation of MB aqueous solutions under visible irradiation. Compared with commercial P25 TiO_2, binary NiFe mixed-metal oxides, pure metal oxide particles (NiO, CoO and Fe_2O_3) and other ternary mixed-metal oxides, the NiCoFe-MMOs exhibit a higher degradation efficiency in degrading organic pollutants under visible irradiation. The photodegradation mechanism was proposed as well.

2. Experimental procedures

2.1 Materials

Nickel nitrate [$Ni(NO_3)_2\cdot 6H_2O$], cobalt nitrate [$Co(NO_3)_2\cdot 6H_2O$] and ferric nitrate [$Fe(NO_3)_3\cdot 9H_2O$] were obtained from Sinopharm Chemical Reagent Co., Ltd (AR, Shanghai, China). Urea (NH_2CONH_2) and methylene blue (MB) were purchased from Tianjin Bodi Chemical Reagent Co., Ltd (AR, Tianjin, China). Commercial P25 TiO_2 was purchased from Alfa Co. and used as a reference in the photocatalytic experiments. Phenol, isopropyl alcohol (IPA), *p*-benzoquinone and EDTA-2Na were provided by Chengdu Kelong Co., Ltd (Chengdu, China). Distilled water was used throughout the experiment. All reagents used in this experiment were of analytical grade and used without further purification.

2.2 Catalyst preparation

2.2.1 Preparation of NiCoFe-LDH (NCF-LDH) precursors. Ternary NCF-LDHs were synthesized using a coprecipitation method. A typical synthetic procedure is as follows: the mass of iron nitrate was maintained at 0.9 g and $Ni(NO_3)_2\cdot 6H_2O$, $Co(NO_3)_2\cdot 6H_2O$ and $Fe(NO_3)_3\cdot 9H_2O$ with different $Ni^{2+}/Co^{2+}/Fe^{3+}$ molar ratios were dissolved in 80 mL deionized water to form a clear solution at room temperature. 3.5 g of urea were dissolved in the as-obtained clear solution under vigorous stirring. Then, the mixture was transferred into a Teflon-lined autoclave and thermally treated at 150 °C for 12 h, and then filtered and washed with distilled water until pH = 7. Finally, the as-obtained solid was oven-dried at 60 °C overnight to obtain NCF-LDH precursors with different $Ni^{2+}/Co^{2+}/Fe^{3+}$ (Ni/Co/Fe) molar ratios (*i.e.*, 0.5 : 0.5 : 1, 1 : 1 : 1, 2 : 2 : 1, 1 : 2 : 1, 1.5 : 1.5 : 1, 2 : 1 : 1, 2.5 : 0.5 : 1, 3 : 0 : 1), and these precursors were denoted as NCF-LDH ($q : m : n$); for example, the one with an $Ni^{2+}/Co^{2+}/Fe^{3+}$ molar ratio of 1 : 2 : 1 was denoted as NCF-LDH (1 : 2 : 1) and the one with an $Ni^{2+}/Co^{2+}/Fe^{3+}$ molar ratio of 3 : 0 : 1 was specifically denoted as NiFe-LDH (3 : 1). In addition, the molar ratio of (Ni^{2+}, Co^{2+})/Fe^{3+} was specifically denoted herein as M^{2+}/M^{3+}.

2.2.2 Preparation of NCF-MMOs. The NCF-LDH precursors were calcined in a muffle furnace under air at 600 °C for 4 h, with a constant heating rate of 5 °C min^{-1}. Subsequently, NCF-MMOs were obtained in the furnace by naturally cooling down to room temperature, and these calcined samples were denoted as NCF-MMO ($q : m : n$); for example, the one with the $Ni^{2+}/Co^{2+}/Fe^{3+}$ molar ratio of 1 : 2 : 1 was denoted as NCF-MMO (1 : 2 : 1) and the one with the $Ni^{2+}/Co^{2+}/Fe^{3+}$ molar ratio of 3 : 0 : 1 was specifically denoted as NiFe-MMO (3 : 1). In addition, pure Fe_2O_3, CoO, and NiO metal oxide particles were synthesized in the same manner.

2.3 Characterization

The compositions and crystal phases of the sample were determined with XRD patterns with X-ray diffraction (XRD, Ultima

 This journal is © The Royal Society of Chemistry 2018

Published on 25 June 2018. Downloaded by University of Tennessee at Knoxville on 9/5/2018 8:48:37 PM.

IV, Rigaku, Japan) with 2θ ranging from 10° to 70°, using Cu Kα radiation (λ = 0.1540 nm). Fourier transform infrared spectroscopy (FT-IR) spectra were obtained using KBr pellets on a Fourier transform infrared spectrometer (FT-IR, Nicolet 380, Thermo, America). The elemental composition of samples was examined using an ESCALAB 250Xi X-ray photoelectron spectroscope (XPS, Thermo Scientific, USA) with monochromatic Al K-Alpha radiation (150 W, 15 kV, and 1486 eV). The morphological features of the samples were investigated using scanning electron microscopy (SEM, SU-70, Hitachi, Japan) and transmission electron microscopy (TEM, JEM-2100F). The specific surface area was calculated using the Brunauer–Emmett–Teller (BET, Tristar II 3020, Micromeritics, America) method. The band gaps of the products were determined from the UV–Vis absorption spectrum on a UV–Vis diffuse reflectance spectrophotometer (UV–Vis DRS, UV9000, METASH, China).

2.4 Photocurrent response test

The photocurrent response of the as-prepared NCF-MMOs was measured with an electrochemical workstation (Autolab, Metrohm Co. Ltd) using a three electrode system. A 20 mg sample was coated on foamed nickel with a 4 cm^2 surface as a working electrode, a platinum electrode as a counter electrode and a saturated calomel electrode as a reference electrode. In detail, the photocurrent response tests were conducted in an electrolyte solution of 1 mol L^{-1} Na_2SO_4. During the test process, a 200 W xenon lamp served as the light source with 15 cm distance from the electrodes.

2.5 Photocatalytic activity performance test

The photocatalytic activity of NCF-MMOs with different molar ratios was monitored by the degradation of MB (50 mg L^{-1} solution). A 200 W xenon lamp with λ = 320–1100 nm was used as the simulated sunlight source. In order to exclude the effects of UV light, a layer of UV-blocking glass was added in the direction of the xenon lamp illuminating the reaction vessel. NiFe-MMO, pure Fe_2O_3, CoO, NiO metal oxide particles and P25 TiO_2 were considered as the reference samples. For each run, 0.05 g catalyst was added into 200 mL MB solution and stirred for 1 h in the dark to establish an adsorption/desorption equilibrium. During irradiation, the catalyst was maintained in a suspension state by a mechanical agitator. The samples (2 ml each time) for analysis were extracted through a pipette every 30 min and centrifuged immediately. After that, the filtrates were tested by measuring the absorbance at 664 nm using a UV-9000 UV–Vis spectrophotometer to determine the concentration of MB. In contrast, the blank experiments, *i.e.*, without a catalyst or in the dark, were carried out under the same conditions. The degradation of the non-dye pollutant phenol was similar to the MB degradation test procedure, but there were two differences. The initial concentration of phenol was 20 mg L^{-1} and its maximum absorption wavelength was 270 nm.

3. Results and discussion

3.1 Characterization of the products

In order to determine the suitable M^{2+}/M^{3+} molar ratio, the NCF-LDH samples were synthesized with different M^{2+}/M^{3+} molar ratios but keeping other conditions constant. Fig. 1 shows the XRD patterns for these samples with different M^{2+}/M^{3+} molar ratios. The diffraction peaks at 2θ = 11.6°, 23.4°, 34.4°, 39.0°, 46.5°, 60.5° and 61.2° can be assigned to the (003), (006), (012), (015), (018), (110) and (113) reflections of LDH, respectively, which is a characteristic of a layered structure.[41,42] They are consistent with the standard card JCPDS-40-0216 and belong to a hexagonal system.[43] Although all the samples exhibit the characteristic diffraction peaks of layered hydrotalcite-like materials, the peak widths and crystallite sizes are different. The broadness of the diffraction peaks is related to a decrease in the crystallite size; the crystallite size of the as-prepared samples is estimated using the Scherrer formula (1)[44]

$$D = k\lambda/(\beta \cos \theta) \quad (1)$$

where D is the crystallite size, k = 0.89 (the Scherrer constant), λ is the wavelength of the Cu Kα radiation (λ = 0.15406 nm), β is the width of the peak (full width at half maximum (FWHM)), and θ is the diffraction angle. The average crystallite size of the sample with M^{2+}/M^{3+} = 3 : 1 estimated using the Scherrer formula from its XRD patterns is ~17.7 nm (D_{003}), whereas those of the samples with M^{2+}/M^{3+} = 1 : 1, 2 : 1 and 4 : 1 are ~13.9, 16.8 and 16.3 nm, respectively. In general, the larger crystallite size leads to a better crystal state of the sample.[45] Besides, the intensity of the characteristic peaks of the sample with M^{2+}/M^{3+} = 1 : 1 is relatively weak and there are many interference peaks of the sample with M^{2+}/M^{3+} = 2 : 1 and 4 : 1. Only the sample with M^{2+}/M^{3+} = 3 : 1 showed much narrower and sharper peaks than the others. Hence, we can conclude that M^{2+}/M^{3+} = 3 : 1 was the best metal molar ratio for synthesizing the NCF-LDHs.

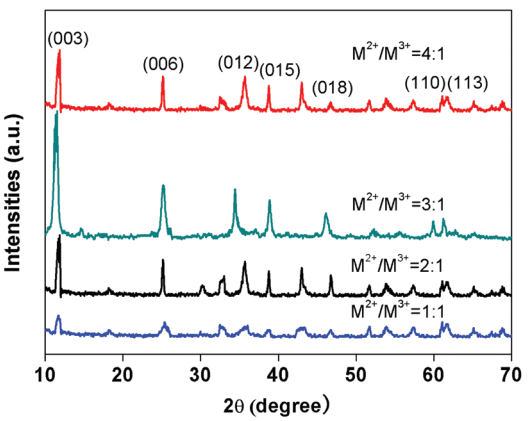

Fig. 1 XRD patterns of the as-synthesized NCF-LDHs with different M^{2+}/M^{3+} molar ratios (1 : 1, 2 : 1, 3 : 1 and 4 : 1).

Published on 25 June 2018. Downloaded by University of Tennessee at Knoxville on 9/5/2018 8:48:37 PM.

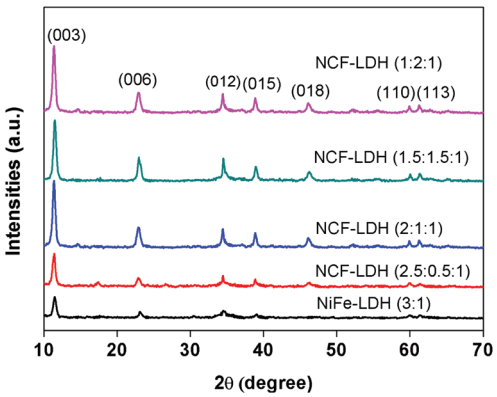

Fig. 2 XRD patterns of NiFe-LDH (3 : 1) and NCF-LDH (1 : 2 : 1, 1.5 : 1.5 : 1, 2 : 1 : 1 and 2.5 : 0.5 : 1) precursors.

As shown in Fig. 2, almost the same typical structures are observed in the XRD patterns of NiFe-LDH (3 : 1) and NCF-LDH precursors (M^{2+}/M^{3+} = 3 : 1). No diffraction peaks corresponding to cobalt compounds are observed, suggesting that the Co^{2+} ions are well dispersed into the NiFe-LDH lattice. Moreover, the NCF-LDHs become dominant compared with the NiFe-LDH, resulting in a well- crystalline product. It is plausible that the incorporation of Co^{2+} results in strong electrostatic interaction between the host layer and guest carbonate to improve crystallinity.[46]

Fig. 3 shows the XRD patterns of the NCF-MMOs obtained from NCF-LDH precursors calcined at 600 °C. After calcination, the NCF-MMOs exhibit the cubic NiO phase with reflections at about 2θ = 37.2°, 43.3°, 62.8° and 75.4°, in accordance with JCPDS-44-1159. The diffraction reflections around 2θ = 30.2°, 35.6° and 43.3° correspond to the crystal of Fe_2O_3 maghemite-C (JCPDS-39-1346). The diffraction peaks of 36.4°, 42.4° and 75.1° can be assigned to the face-centered cubic CoO structure (JCPDS-71-1178).[47] Besides the above phases, the characteristic diffraction peaks can also be assigned to the spinel type cubic structure of Co_3O_4 with the *Fd3m* (227) space group (JCPDS-43-1003).[48] This phenomenon mainly originated from the unintended thermo-induced effect due to the alternation between Co^{2+} cations and O^{2-} anions from one plane to another, which ultimately gave Co_3O_4.[47] It is worth mentioning

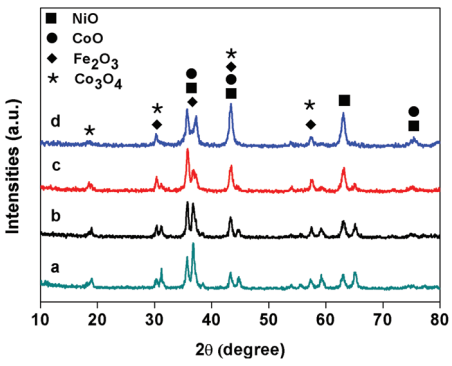

Fig. 3 XRD patterns of (a) NCF-MMO (1 : 2 : 1), (b) NCF-MMO (1.5 : 1.5 : 1), (c) NCF-MMO (2 : 1 : 1) and (d) NCF-MMO (2.5 : 0.5 : 1).

that the remaining crystal phase had not been detected because it might overlap with the main phase.[49]

To reveal the specific surface area and porosity of the as-prepared samples, BET measurement was carried out (Fig. 4). The shape of the isotherm seems to be close to the type IV isotherm according to the IUPAC classification, which is a typical characteristic of mesoporous materials.[50] The samples calcined at 600 °C present large specific surface areas (66.9–93.8 $m^2\ g^{-1}$). It is worth mentioning that NCF-MMO (1 : 2 : 1) has a lower specific surface area than NCF-MMO (1.5 : 1.5 : 1) and NCF-MMO (2 : 1 : 1), which may be attributed to a higher crystalline structure in accordance with the XRD observations.[46] The specific surface area and pore performance data of the samples are listed in Table 1. It is found that the samples have a primary pore size of around 7–15 nm, varying with the ratio of Ni/Co/Fe. Furthermore, the pore size and pore volume of ternary NCF-MMOs are generally larger than those of the binary NiFe-MMO (3 : 1).

The FT-IR spectra of the as-synthesized LDH samples, as shown in Fig. 5, are very similar to those generally reported for hydrotalcite-like compounds. The bands around 3410 cm^{-1} can be ascribed to the stretching mode of the OH group with hydrogen bonding and of interlayer water molecules.[51] Similarly, the band observed at 1630 cm^{-1} can be attributed to the bending mode of crystalline water.[52] The band at around 1382 cm^{-1} corresponds to the stretching vibration of the CO_3^{2-} anions (caused by urea decomposition during the synthesis of the samples) in the LDH interlayer. The bands at approximately 835 and 570 cm^{-1} arise from the metal–oxygen bond (M–O, M–O–M and M–OH) vibrations in the LDHs.[53,54]

The morphology of the as-prepared NCF-MMOs was characterized by SEM. The synthesized NCF-MMO (1 : 2 : 1) shows regular cubes with an edge length of about 2 μm (Fig. 6A). Irregular multilateral geometries and some fragments appeared for the molar ratio of Ni/Co/Fe = 1.5 : 1.5 : 1 (Fig. 6B). It can be seen that the morphology of NCF-MMO (2 : 1 : 1) collapses from a specific structure and becomes irregular aggregates after calcination at 600 °C (Fig. 6C). And in Fig. 6D, there is an obvious morphology change from aggregates to a rod-like structure for the as-synthesized NCF-MMO (2.5 : 0.5 : 1). The change of morphology seems to be a powerful explanation for NCF-MMO (2 : 1 : 1) having a large specific surface area and small pore size, while NCF-MMO (2.5 : 0.5 : 1) has the opposite result in accordance with the specific surface area and pore performance data observed in Table 1.

From the observed XRD, BET and SEM results, the SEM images of NCF-LDH (1 : 2 : 1) with good crystallinity, a relatively ideal specific surface area and a regular morphology are further presented in Fig. 7. It can be seen that the samples before calcination are formed by the aggregation of many regular cubes, and the edge length of each cube is about 1.5 μm (Fig. 7A). It is worth noting that the surface of NCF-LDH is relatively smooth and some clusters appear before calcination (Fig. 7B), which further proves that the samples are well-crystalline in accordance with the XRD observations. After calcination at 600 °C, the edge length of each cube is slightly

 This journal is © The Royal Society of Chemistry 2018

Published on 25 June 2018. Downloaded by University of Tennessee at Knoxville on 9/5/2018 8:48:37 PM.

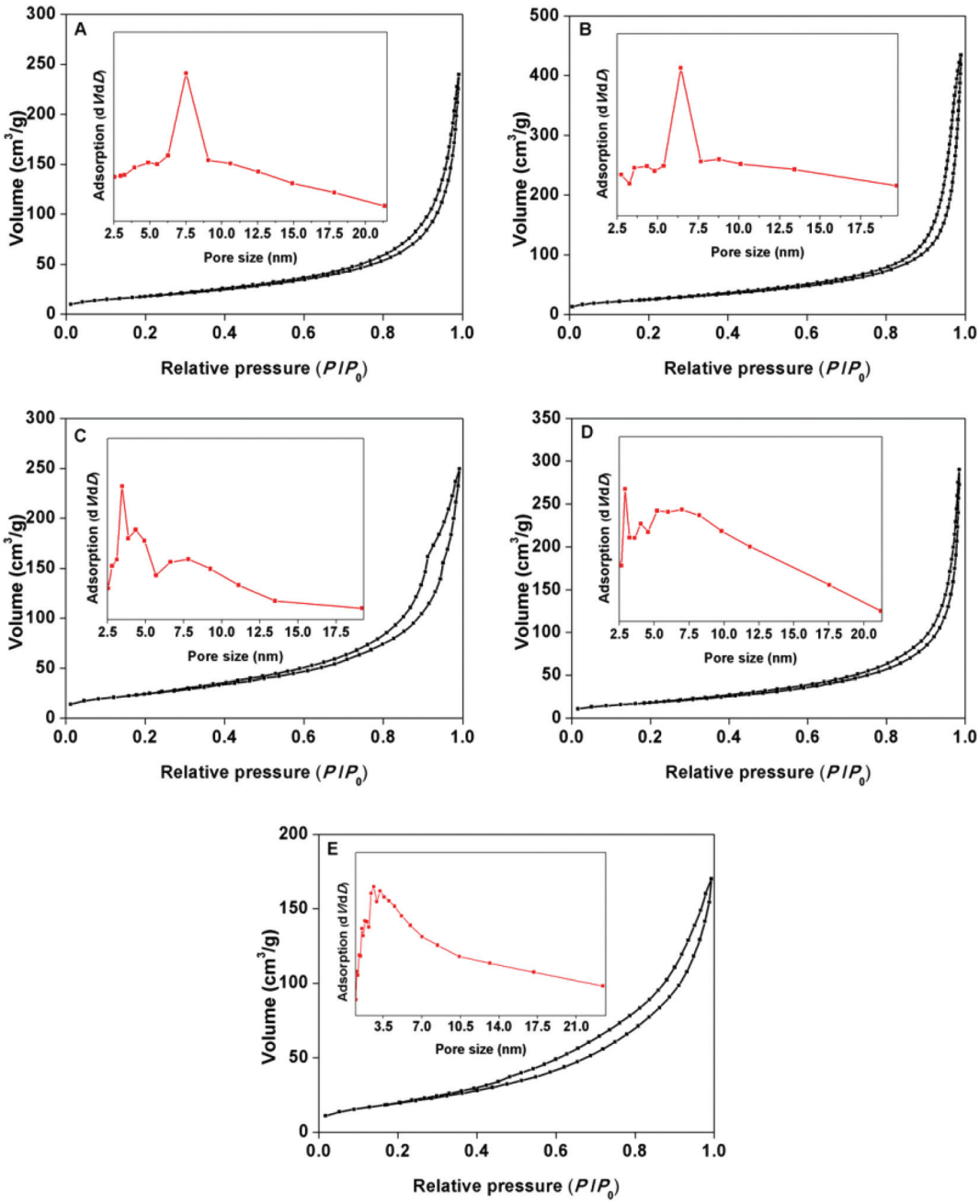

Fig. 4 N_2 sorption isotherms and pore size distribution of (A) NCF-MMO (1 : 2 : 1), (B) NCF-MMO (1.5 : 1.5 : 1), (C) NCF-MMO (2 : 1 : 1), (D) NCF-MMO (2.5 : 0.5 : 1) and (E) NiFe-MMO (3 : 1).

increased to 2 μm, and the surface of the sample becomes rougher (Fig. 7C). It can be clearly seen that each cube is accumulated with many fine particles with a size of ~130 nm (Fig. 7D). The increased edge length and rough surface after calcination may be attributed to the interlayer residual water molecules, which are volatilized in the form of gas during the calcination process. The EDX pattern further confirms the presence of Ni, Co, Fe and O elements in NCF-MMO (1 : 2 : 1) (Fig. 7E).

The morphology of NCF-MMO (1 : 2 : 1) was further observed using TEM. Fig. 8A and B clearly demonstrate that the samples are formed by the aggregation of regular cubes, and each cube is accumulated with many fine particles with a size of ~130 nm, which are consistent with the observations by SEM. The high-resolution transmission electron microscopy (HRTEM) image of NCF-MMO (1 : 2 : 1) is shown in Fig. 8C, and well-defined lattice planes are observed, which indicate the high crystallinity of the samples. The lattice fringes with an interplanar distance of 0.260 and 0.280 nm can be ascribed to the (001) and (220) planes of CoO and Co_3O_4 phases, respectively.[37] Besides, the spacings of 0.238 and 0.268 nm correspond to the (200) plane of NiO and the (104) plane of

Published on 25 June 2018. Downloaded by University of Tennessee at Knoxville on 9/5/2018 8:48:37 PM.

Table 1 The specific surface area and pore performance data of NCF-MMOs and NiFe-MMO

Samples	Surface area S_{BET} [a] ($m^2\ g^{-1}$)	Pore size[b] (nm)	Pore volume[c] ($cm^3\ g^{-1}$)
NCF-MMO (1 : 2 : 1)	87.1	11.10	0.37
NCF-MMO (1.5 : 1.5 : 1)	93.8	14.38	0.68
NCF-MMO (2 : 1 : 1)	90.3	8.59	0.39
NCF-MMO (2.5 : 0.5 : 1)	66.9	13.48	0.45
NiFe-MMO (3 : 1)	74.3	7.95	0.28

[a] The specific surface areas (S_{BET}) were calculated using the nitrogen adsorption data according to a BET method. [b] Pore size was estimated by applying the BJH method to the desorption branch of the isotherms. [c] Total pore volume (V_p) was estimated from the adsorption data at $p/p_0 = 0.99$.

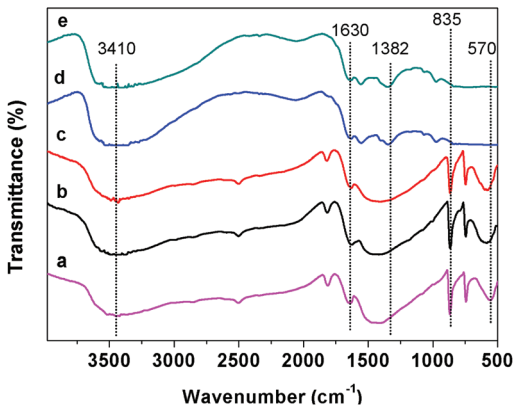

Fig. 5 FT-IR spectra of (a) NiFe-LDH (3 : 1), (b) NCF-LDH (1 : 2 : 1), (c) NCF-LDH (1.5 : 1.5 : 1), (d) NCF-LDH (2 : 1 : 1) and (e) NCF-LDH (2.5 : 0.5 : 1).

Fe_2O_3, respectively. The selected area electron diffraction (SAED) pattern (Fig. 8D) suggests that the mixed-metal oxides are polycrystalline,[55] which is supported by low peak intensities obtained in the XRD diffractograms.

The chemical composition and elemental valence of NCF-MMO (1 : 2 : 1) were confirmed by XPS measurements, as shown in Fig. 9. The fully scanned spectrum (Fig. 9A) shows that the main elements Ni, Co, Fe and O exist in NCF-MMO (1 : 2 : 1). The C element can be ascribed to the instrument measurement because the binding energy for the C 1s peak at 284.8 eV is used as the reference for calibration,[56] and the O 1s peak localized at 530.5 eV can be ascribed to O^{2-}.[57] In Fig. 9B, the Ni $2p_{3/2}$ signal appears at 854.8 eV, and the peak at 872.7 eV comes from Ni $2p_{1/2}$, which can be ascribed to the Ni^{2+} species.[58] The Co 2p spectrum (Fig. 9C) displays two contributions in the Co $2p_{3/2}$ region and two contributions in the Co $2p_{1/2}$ region. The peaks at binding energies 782.3 and 797.0 and 780.5 eV are assigned to Co^{3+} and Co^{2+} species, and the peak at 795.7 eV is assigned to both Co^{2+} and Co^{3+} species. This result further proves that Co is present in both CoO and Co_3O_4 compounds and is consistent with the XRD results. Three peaks around 711.0, 713.3 and 724.7 eV can be assigned to Fe $2p_{3/2}$ and Fe $2p_{1/2}$ (Fig. 9D), which indicates the existence of Fe^{3+} in NCF-MMO (1 : 2 : 1).[59]

3.2 Photocatalytic activity

Fig. 10A shows the UV-Vis absorption spectra of the as-prepared samples. It is seen that the spectral intensity of NCF-MMOs is higher than that of NiFe-MMOs because of the incorporation of Co^{2+} cations, and the NCF-MMOs have a better stability of absorbance, and the absorption edge intensity is extended up to *ca.* 750 nm, covering the full visible light

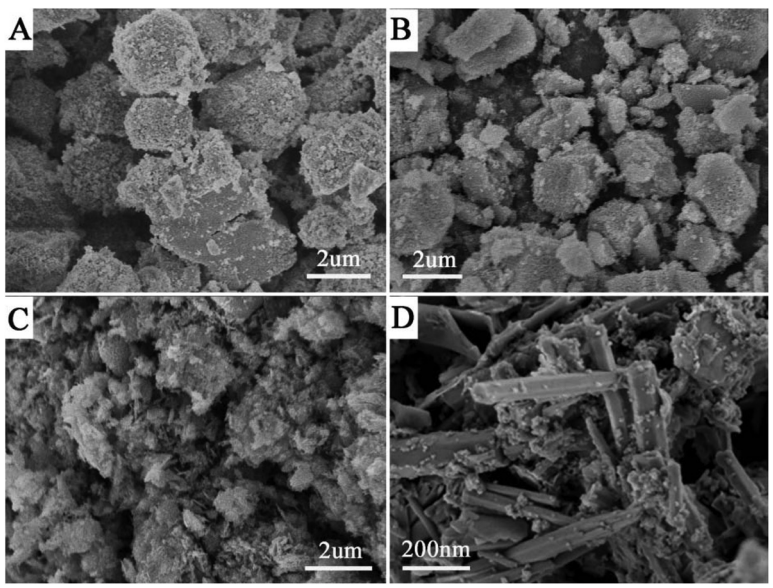

Fig. 6 SEM images of (A) NCF-MMO (1 : 2 : 1), (B) NCF-MMO (1.5 : 1.5 : 1), (C) NCF-MMO (2 : 1 : 1) and (D) NCF-MMO (2.5 : 0.5 : 1).

 This journal is © The Royal Society of Chemistry 2018

Published on 25 June 2018. Downloaded by University of Tennessee at Knoxville on 9/5/2018 8:48:37 PM.

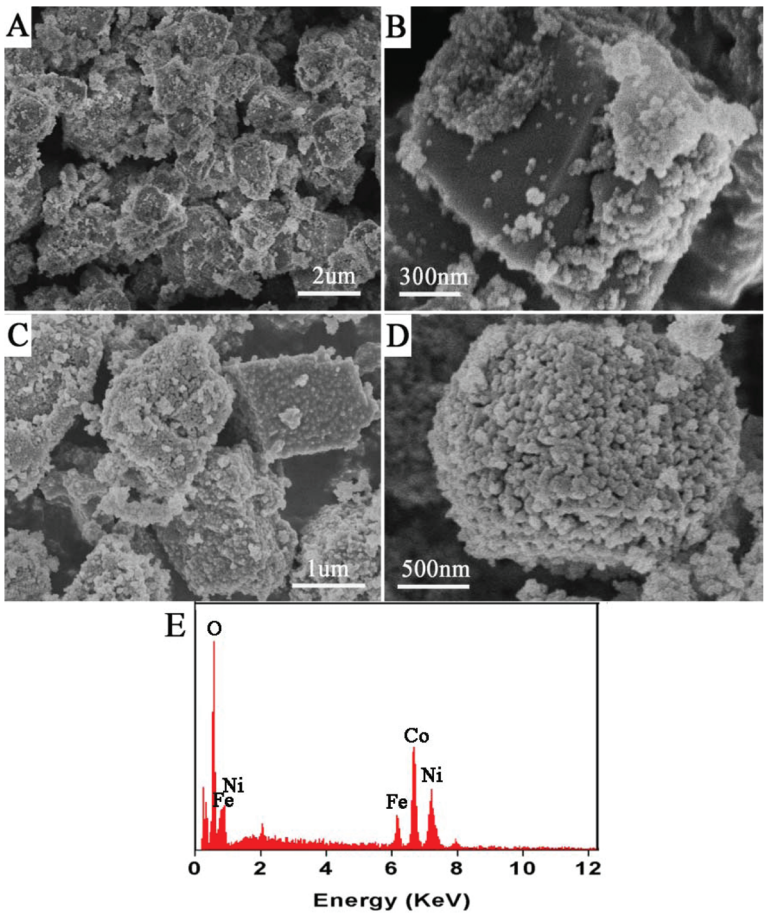

Fig. 7 SEM images of (A, B) NCF-LDH (1 : 2 : 1) and (C, D) NCF-MMO (1 : 2 : 1) along with the EDX measurement of (E) NCF-MMO (1 : 2 : 1).

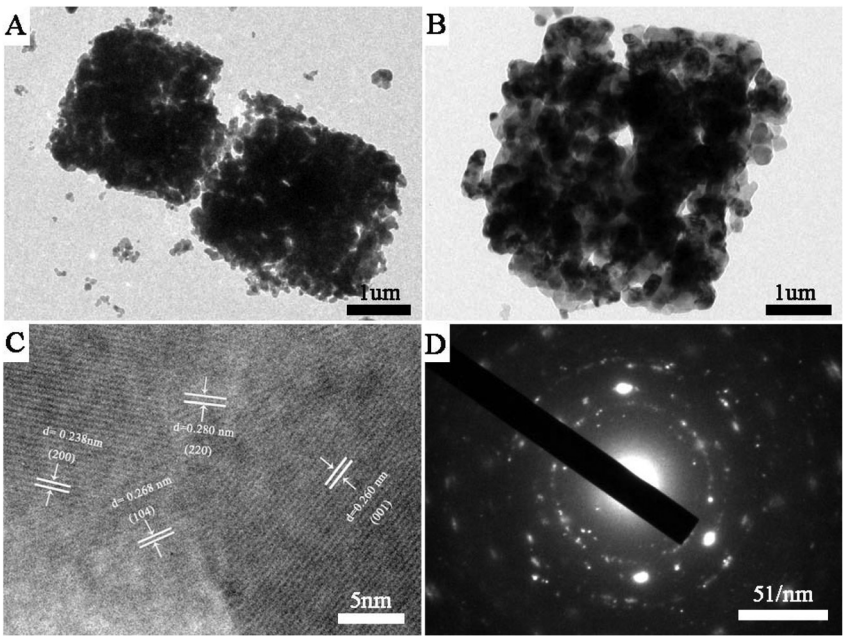

Fig. 8 TEM images (A and B), HRTEM image (C) and SAED pattern (D) of NCF-MMO (1 : 2 : 1).

Published on 25 June 2018. Downloaded by University of Tennessee at Knoxville on 9/5/2018 8:48:37 PM.

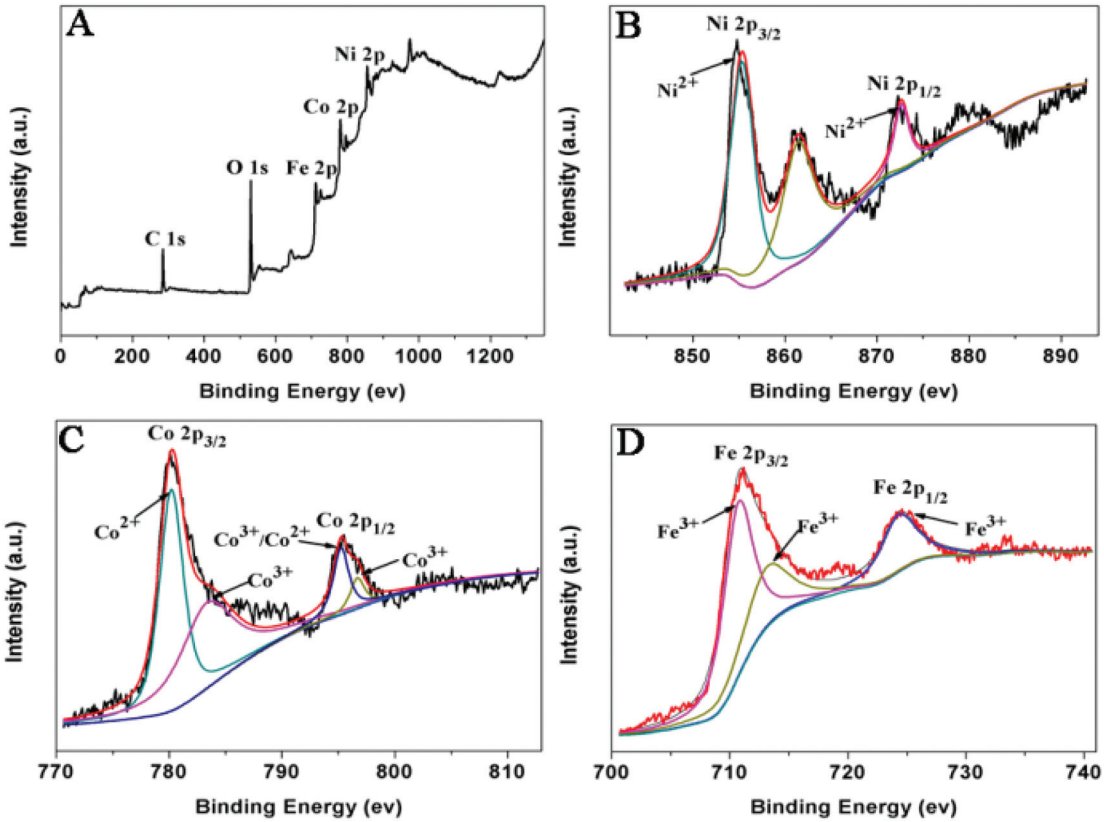

Fig. 9 XPS full survey spectra of NCF-MMO (1 : 2 : 1) (A), the XPS spectra of Ni 2p (B), Co 2p (C) and Fe 2p (D) in NCF-MMO (1 : 2 : 1).

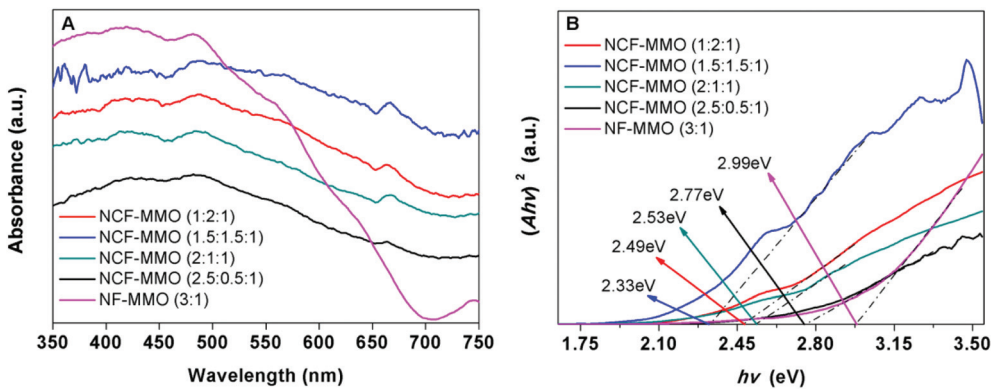

Fig. 10 UV-vis absorption spectra (A) of NiFe-MMOs and NCF-MMOs with different molar ratios and the plotting of $(Ah\nu)^2$ *vs.* $h\nu$ based on the direct transition (B).

spectrum.[60] Using the absorption spectrum data, the band gap of the prepared samples can be estimated using eqn (2):[61]

$$(Ah\nu)^2 = K(h\nu - E_g) \quad (2)$$

where A is the absorption coefficient, $h\nu$ is the photon energy, E_g is the band gap energy for direct transitions, and K is a proportionality constant. The normalized graphs of $(Ah\nu)^2$ for the photon energy of the as-prepared samples are shown in Fig. 10B. All the NCF-MMO samples exhibit a relatively lower band gap energy than NiFe-MMO. The lower band gap may be attributed to the addition of Co^{2+}, and the band gap value of pure CoO (~2.6 eV)[37] is smaller than that of NiO (~3.7 eV).[62] The NCF-MMOs are thus expected to show better photocatalytic activity than NiFe-MMO under visible light.

The comparative results of MB degradation under different experimental conditions are shown in Fig. 11. During the first 1 h of the tests (corresponding to the time −1 to 0 h), there was no light illumination and the MB solution was stirred with different catalysts. The initial decrease of the dye concen-

 This journal is © The Royal Society of Chemistry 2018

Published on 25 June 2018. Downloaded by University of Tennessee at Knoxville on 9/5/2018 8:48:37 PM.

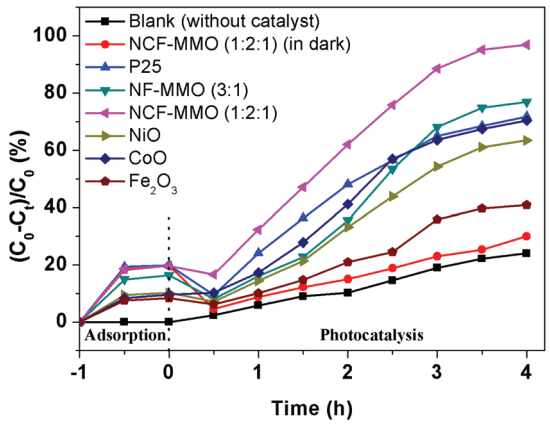

Fig. 11 Comparison of MB degradation over Degussa P25 TiO_2, NiO, CoO, Fe_2O_3, NiFe-MMO (3 : 1), NCF-MMO (1 : 2 : 1) and only light irradiation (without catalyst) or only catalyst (in the dark).

tration may be due to the relatively high specific surface area and abundant pore structure that result in the rapid adsorption of MB on different sample surfaces. All adsorption efficiencies were below 20% for half an hour and tended to reach equilibrium in 1 h. In order to eliminate the interference of adsorption, the dye concentration after adsorption for 1 h was taken as the new initial concentration for photocatalysis. After illumination for 4 h, MB had a degradation efficiency of ~24.2% and ~29.7% upon exposure to visible light irradiation without adding any solid catalysts and without any visible light irradiation, respectively. This indicates that both photolysis and catalysts are beneficial to the degradation of MB. It is obvious that NCF-MMO (1 : 2 : 1) shows a better photocatalytic performance (96.82%) than NiFe-MMO (3 : 1) (76.88%), commercial P25 TiO_2 (71.80%), pure Fe_2O_3 particles (40.82%), NiO particles (63.45%) and CoO particles (70.39%). This result may be attributed to the appearance of fine particles, which increases the specific surface area of the catalytic substance and the active sites of the degradation of MB. A similar phenomenon has been observed in the recent work by Zhang *et al.*[63] It is deduced that the inclusion of Co^{2+} increases the capability for the degradation of MB, in agreement with the observations of Chowdhury *et al.*[64]

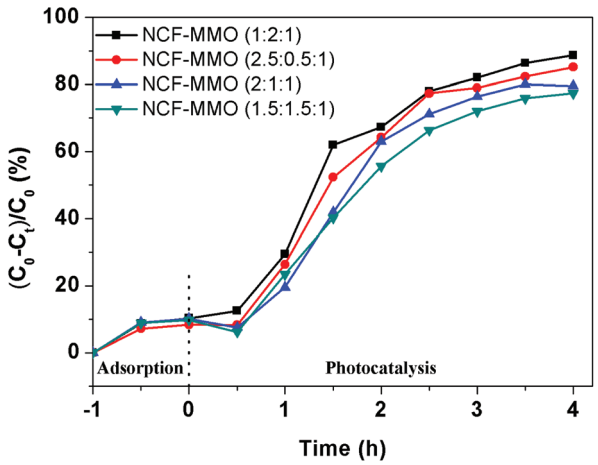

Fig. 12 Degradation of phenol with NCF-MMOs.

The degradation of the non-dye pollutant phenol was also performed. As can be seen in Fig. 12, after illumination for 4 h under a certain simulated visible light, the photocatalytic performances of NCF-MMO (1 : 2 : 1), NCF-MMO (2.5 : 0.5 : 1), NCF-MMO (2 : 1 : 1) and NCF-MMO (1.5 : 1.5 : 1) were 88.64%, 86.12%, 80.56%, and 76.34%, respectively. It can be seen that NCF-MMOs not only show a better photocatalytic performance for the dye pollutant MB but also have high degradation activity for the non-dye pollutant phenols.

Since NCF-MMO (1 : 2 : 1) has a stronger degradation effect on MB, in order to better research the photocatalytic efficiency of the as-prepared ternary NCF-MMOs, the photocatalytic degradation kinetics of MB was investigated. As can be seen in Fig. 13A, the photocatalytic degradation process fits well with pseudo-first-order kinetics as shown in eqn (3):[65]

$$\ln(C_0/C) = kt \quad (3)$$

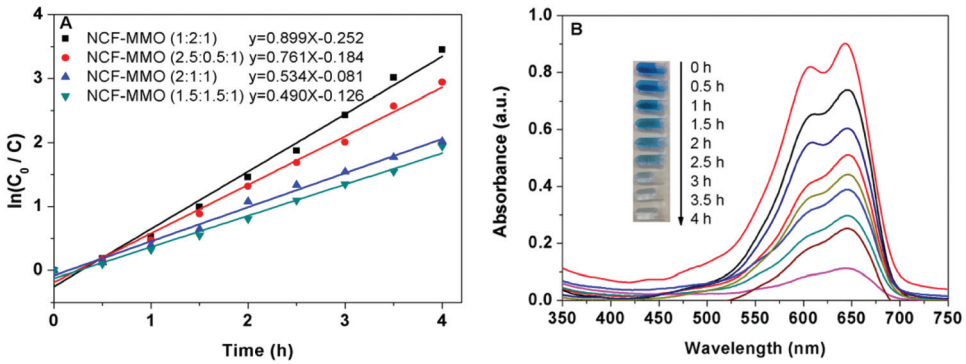

Fig. 13 The photodegradation kinetic curves (A) of NCF-MMO (1 : 2 : 1, 1.5 : 1.5 : 1, 2 : 1 : 1 and 2.5 : 0.5 : 1) and the time-dependent UV-vis absorption spectra (B) of MB with the use of NCF-MMO (1 : 2 : 1).

Published on 25 June 2018. Downloaded by University of Tennessee at Knoxville on 9/5/2018 8:48:37 PM.

Table 2 The kinetic constant k of MB photocatalytic degradation affected by different NCF-MMO catalysts

Samples	K (h^{-1})	R^2	Efficiency[a] (%)
NCF-MMO (1 : 2 : 1)	0.899	0.9871	96.82
NCF-MMO (1.5 : 1.5 : 1)	0.490	0.9881	85.60
NCF-MMO (2 : 1 : 1)	0.534	0.9900	86.72
NCF-MMO (2.5 : 0.5 : 1)	0.761	0.9901	94.66

[a] The degradation efficiency of the MB dye using different samples under visible light irradiation for 4 h.

where C_0 is the initial concentration of MB, C is the concentration of MB at the reaction time t, k is the reaction rate constant and t is the reaction time.

The reaction rate constant (k) and correlation coefficient (R^2) for the degradation of MB under visible light illumination with NCF-MMO catalysts with different Co contents are shown in Table 2. These results confirmed that the photocatalytic degradation rate was much higher in the case of NCF-MMO (1 : 2 : 1) compared to the value obtained with other NCF-MMO catalysts. The time-dependent UV-Vis absorption spectra of MB with the use of NCF-MMO (1 : 2 : 1) are also shown in Fig. 13B, and the degradation rate of the MB aqueous solutions was more than 96% under visible irradiation after 4 h. The digital photograph (Fig. 13B, inset) shows that after 4 h, the MB aqueous solution was entirely decolorized, suggesting the excellent photocatalytic activity of NCF-MMO (1 : 2 : 1).

Based on the above analysis, the enhanced photocatalytic activity for the decomposition of MB is probably due to the fast interfacial transfer of photogenerated charge carriers within NCF-MMO (1 : 2 : 1) and subsequent effective charge separation. In order to study the separation efficiency of photo-induced charge carriers of ternary NCF-MMO photoelectrodes, the influence of different molar ratios of NCF-MMOs on the visible light photocurrent response is also evaluated and shown in Fig. 14. The photocurrent measurement against time

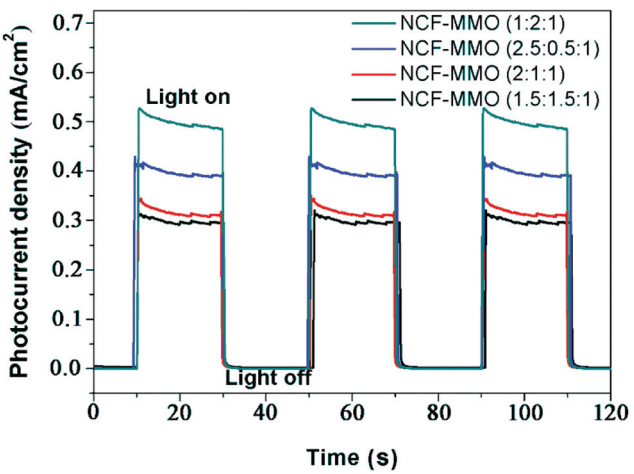

Fig. 14 The photocurrent response of NCF-MMO (1 : 2 : 1, 1.5 : 1.5 : 1, 2 : 1 : 1 and 2.5 : 0.5 : 1) in the 1 M Na_2SO_4 electrolyte under visible light irradiation.

Table 3 Comparison of the photocatalytic activity of several ternary mixed-metal oxides

Photocatalysts	Morphology, dosage	Dye	Catalytic efficiency	Ref.
MgZnIn-MMO	Aggregates 0.05 g	MB 10 mg L^{-1}, 100 mL	98% after 5 h	46
ZnAlIn-MMO	Aggregates 0.05 g	MB 5 mg L^{-1}, 100 mL	Under 94% after 4 h	66
ZnNiFe-MMO	Nanoparticles 0.3 g	MO 5×10^{-5} M, 50 ml	93.1% after 4 h	67
NiCoFe-MMO	Regular cubes 0.05 g	MB 50 mg L^{-1}, 200 mL	96.82% after 4 h	This work

of different photoelectrodes was recorded *via* several on–off cycles of a periodic 200 W xenon lamp light irradiation pulse of 20 s. Clearly, the NCF-MMO (1 : 2 : 1) photoelectrode exhibited a stronger transient photocurrent response under xenon illumination, which was consistent with the photocatalytic degradation effect. It reveals that the NCF-MMO (1 : 2 : 1) photoelectrode has a higher efficiency of electron–hole separation and lower rate of charge carrier recombination.

Table 3 lists the comparison of morphology, dosage and photocatalytic activity for various ternary mixed-metal oxides. In this work, NiCoFe-MMO not only has a specific morphology but also shows a good catalysis effect (it can catalyze more organic dye with the same amount of photocatalysts).

In addition to the high photocatalytic activity, the durability of NCF-MMO (1 : 2 : 1) for MB degradation is also studied and shown in Fig. 15. After being reused 5 times, no obvious decrease of photocatalytic activity can be observed, which is indicative of its high stability and lasting activity under continuous visible-light irradiation. However, after being reused 7 times, the degradation efficiency of the catalyst decreased from 96.82% to 83.47%. The decrease in the photocatalytic activity may be attributed to the inorganic ions adsorbed onto the NCF-MMO (1 : 2 : 1) photocatalysts during the process of the degradation of MB.[68]

3.3 Photodegradation mechanism

It is well-known that radicals (*e.g.*, $^{\bullet}OH$, $O_2^{\bullet-}$, and h^+) are generated during the irradiation process and are responsible for dye degradation.[69,70] In order to determine which radical plays a dominant role, radical scavenging experiments were carried out. EDTA-2Na is a hole-capturer. From the results shown in Fig. 16, it can be seen that the final degradation efficiency has almost no obvious change under visible light irradiation for 4 h when adding 1 mM EDTA-2Na, which proves that the hole (h^+) does not play a major role in the photodegradation of MB. *p*-Benzoquinone and isopropyl alcohol (IPA) are usually $O_2^{\bullet-}$ and $^{\bullet}OH$ scavengers, respectively. There was a slight reduction to 82.42% on the addition of 1 mM *p*-benzoquinone compared to that without the addition of any radical scavengers (96.82%). However, it is found that the degradation of MB sig-

 This journal is © The Royal Society of Chemistry 2018

Published on 25 June 2018. Downloaded by University of Tennessee at Knoxville on 9/5/2018 8:48:37 PM.

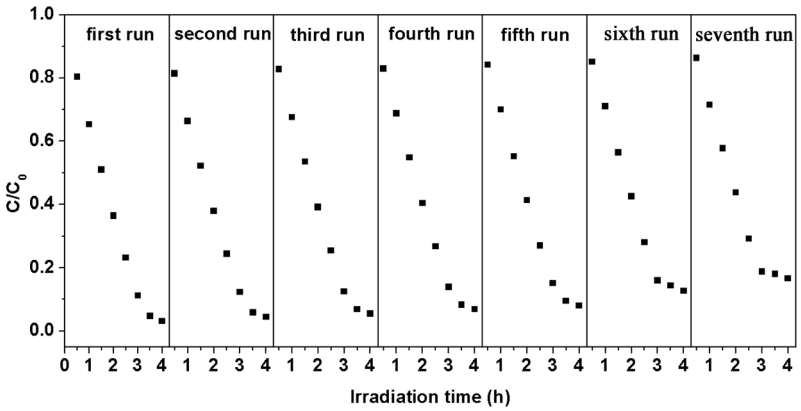

Fig. 15 Recycling use of NCF-MMO (1 : 2 : 1) for dye degradation.

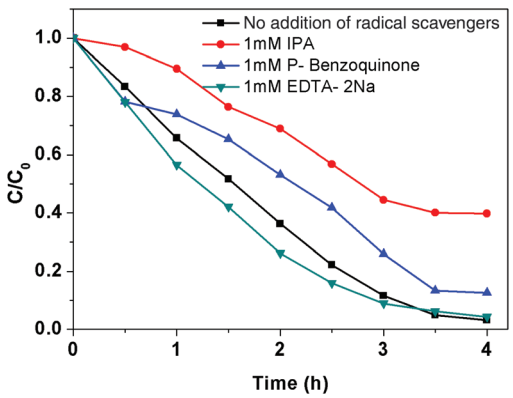

Fig. 16 Effect of radical scavengers (IPA, *p*-benzoquinone and EDTA-2Na) on the photodegradation of MB in an aqueous solution in the presence of NCF-MMO (1 : 2 : 1).

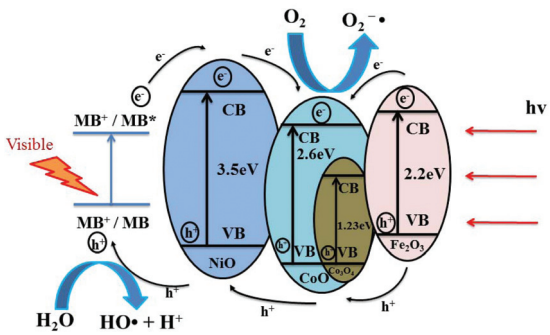

Fig. 17 Mechanism scheme for MB degradation using NCF-MMO (1 : 2 : 1).

nificantly decreased to 58.16% on the addition of 1 mM IPA. Hence, $^{\bullet}OH$ is mostly responsible for MB degradation.

Based on the above experimental results, the photodegradation mechanism of MB can be explained and is schematically shown in Fig. 17. The detailed reaction process can be represented in eqn (4)–(11).

$$MB + \text{visible light} \rightarrow MB^{*} \quad (4)$$

$$MB^{*} + NiO \rightarrow MB^{+} + NiO\ (e^{-}) \quad (5)$$

$$Co_3O_4 + \text{visible light} \rightarrow Co_3O_4\ (e^{-}) + Co_3O_4\ (h^{+}) \quad (6)$$

$$CoO/Fe_2O_3 + \text{visible light} \rightarrow CoO/Fe_2O_3\ (e^{-}) + CoO/Fe_2O_3\ (h^{+}) \quad (7)$$

$$e^{-} + O_2 \rightarrow O_2^{\bullet -} \quad (8)$$

$$h^{+} + H_2O \rightarrow {}^{\bullet}OH + H^{+} \quad (9)$$

$$MB^{+} + O_2^{\bullet -} \rightarrow \text{degradation products} \quad (10)$$

$$MB + {}^{\bullet}OH \rightarrow \text{degradation products} \quad (11)$$

Under visible light irradiation, the effective light is absorbed by MB and an excited state (MB*) forms upon light excitation (eqn (4)). The photo-generated electrons (e^{-}) could be injected into the conduction band (CB) of NiO on the basis of the similar potentials between the excited MB^{+}/MB^{*} (−0.75 V *vs.* NHE) and the CB of NiO (−0.50 V *vs.* NHE), and thus the oxidized dye (MB^{+}) was formed (eqn (5)).[71,72] At the same time, the ground state electrons are excited from the valence band of the Co_3O_4 semiconductor to produce electrons and holes (eqn (6)). More importantly, when p-CoO is loaded with n-Fe_2O_3 nanoparticles, a p–n heterojunction was formed between the two semiconductors, and the heterostructures of CoO/Fe_2O_3 could promote efficient electron transfer *via* the interfaces (eqn (7)).[73,74] All excited electrons are transferred into the CB of CoO through the heterojunctions since CoO has a less negative CB potential (−0.11 V *vs.* NHE). Thus, it promotes the separation of photogenerated electrons and holes and increases the photo-oxidation efficiency. Accumulated electrons in the conduction band of CoO are transferred to oxygen molecules to form a superoxide radical anion ($O_2^{\bullet -}$), which contributes to dye degradation (eqn (8) and (10)).[75] In addition, there is a relatively high concentration of h^{+} that could capture H_2O to form the hydroxyl radical ($^{\bullet}OH$) (eqn (9)). The ·OH radical with high oxidation ability plays the most important role in the degradation of MB (eqn (11)).[76,77]

Published on 25 June 2018. Downloaded by University of Tennessee at Knoxville on 9/5/2018 8:48:37 PM.

4. Conclusions

In this work, ternary NiCoFe mixed-metal oxides (NCF-MMOs) with large specific surface areas were synthesized *via* a hydrotalcite-like precursor route. The as-synthesized NCF-MMO (1 : 2 : 1) exhibited regular cubes with an edge length of about 2 μm, and each cube was accumulated with many fine particles with a size of ~130 nm. In addition, the NCF-MMOs had a lower band gap and stronger visible light absorption ability than binary NiFe mixed-metal oxides. The photocatalytic degradation efficiency of the MB dye under visible light irradiation for 4 h was 96.82%, which exceeded those of commercial P25 (71.80%), binary NiFe-MMO (76.88%), pure Fe_2O_3 particles (40.82%), NiO particles (63.45%) and CoO particles (70.39%) under the same conditions. In addition, NCF-MMOs not only showed a better photocatalytic performance for the dye pollutant MB but also had a high degradation activity for the non-dye pollutant phenols. The degradation kinetics of MB promoted by the NCF-MMO photocatalysts followed a pseudo-first-order kinetic behavior and the NCF-MMO (1 : 2 : 1) catalyst showed high stability and activity with no obvious changes in the fifth run. The high photocatalytic activity of the sample was attributed to the addition of Co^{2+} and the high activity of ·OH radicals. Thus, this work provides a facile approach to design photocatalysts with structural durability, high efficiency, and lasting reusability and has a high potential application value in terms of dealing with organic dyes. Considering its unique electronic properties, this material can be used for other applications as well such as solar cells,[78] water splitting,[79] as fillers to make functional polymers or carbon nanocomposites,[80,81] power generation,[82] *etc*.

Conflicts of interest

There are no conflicts of interests to declare.

References

1 F. T. Chen, P. F. Fang, Y. P. Gao, Z. Liu, Y. Liu and Y. Q. Dai, *Chem. Eng. J.*, 2012, **204**, 107–113.
2 Y. Guo, Y. Li, X. Lou, J. Guan, Y. Li, X. Mai, H. Liu, C. X. Zhao, N. Wang, C. Yan, G. Gao, H. Yuan, J. Dai, R. Su and Z. Guo, *J. Mater. Sci.*, 2018, DOI: 10.1007/s10853-018-2229-0, in press.
3 H. J. Fan, C. S. Lu, W. L. W. Lee, M. R. Chiou and C. C. Chen, *J. Hazard. Mater.*, 2011, **185**, 227–235.
4 (*a*) Z. Zhao, R. Guan, J. Zhang, Z. Zhao and P. Bai, *Acta Metall. Sin.*, 2017, **30**, 66–72; (*b*) X. Lou, C. Lin, Q. Luo, J. Zhao, B. Wang, J. Li, Q. Shao, X. Guo, N. Wang and Z. Guo, *ChemElectroChem*, 2017, **4**, 3171–3180.
5 X. Wu, J. Song, J. Li, Q. Shao, N. Cao, N. Lu and Z. Guo, *Polymer*, 2017, **124**, 41–47.
6 Y. Kong, Y. Li, G. Hu, J. Lin, D. Pan, D. Dong, E. Wujick, Q. Shao, M. Wu, J. Zhao and Z. Guo, *Polymer*, 2018, **145**, 232–241.
7 Y. Kong, Y. Li, G. Hu, N. Cao, Y. Ling, D. Pan, Q. Shao and Z. Guo, *Polym. Adv. Technol.*, 2018, DOI: 10.1002/pat.4346.
8 H. Kang, Q. Shao, X. Guo, A. Galaska, Y. Liu and Z. Guo, *Eng. Sci.*, 2018, **1**, 78–85, DOI: 10.30919/espub.es.180312, http://www.espublisher.com/.
9 D. Wang, Y. Sun, Q. Shang, X. Wang, T. Guo and H. Guan, *J. Catal.*, 2017, **356**, 32–42.
10 (*a*) L. Zhang, W. Yu, C. Han, J. Guo, Q. Zhang, H. Xie, Q. Shao, Z. Sun and Z. Guo, *J. Electrochem. Soc.*, 2017, **164**, H651–H656; (*b*) L. Zhang, W. Yu, C. Han, J. Guo, Q. Zhang, H. Xie, Q. Shao, Z. Sun and Z. Guo, *J. Electrochem. Soc.*, 2017, **164**, H651–H656; (*c*) L. Zhang, M. Qin, W. Yu, Q. Zhang, H. Xie, Z. Sun, Q. Shao, X. Guo, L. Hao, Y. Zheng and Z. Guo, *J. Electrochem. Soc.*, 2017, **164**, H1086–H1090.
11 L. Zhang, M. Qin, W. Yu, Q. Zhang, H. Xie, Z. Sun, Q. Shao, X. Guo, L. Hao, Y. Zheng and Z. Guo, *J. Electrochem. Soc.*, 2017, **164**, H1086–H1090.
12 J. Ahmad and K. Majid, *Adv. Compos. Hybrid Mater.*, 2018, **1**, 374–388.
13 L. F. Liotta, M. Gruttadauria, G. Di Carlo, G. Perrini and V. Librando, *J. Hazard. Mater.*, 2009, **162**, 588–606.
14 K. Wang, J. Ma, Z. Yao, W. Zhang and S. Komarneni, *Ceram. Int.*, 2016, **42**, 15981–15988.
15 H. Zhao, W. Deng and Y. Li, *Adv. Compos. Hybrid Mater.*, 2018, **1**, 404–413.
16 Z. W. Huang, K. F. Chen, J. H. Zhang, Y. X. Li, H. Wang, D. D. Cui, J. W. Tang, Y. Liu, X. M. Shi, W. Li, D. Liu, R. Chen and R. S. Sucgang, *Stem Cell Rep.*, 2013, **3**, 577–558.
17 D. Wu, X. Zhang, J. Zhu and D. Cheng, *Eng. Sci.*, 2018, **2**, 49–56, DOI: 10.30919/es8d718, http://www.espublisher.com/.
18 J. A. Terrett, J. D. Cuthbertson and V. W. Shurtleff, *Nature*, 2015, **524**, 330–334.
19 Z. Zhao, J. Tian, Y. Sang, A. Cabot and H. Liu, *Adv. Mater.*, 2015, **27**, 2557–2582.
20 S. Mao, R. Bao, D. Fang and J. Yi, *Mater. Res. Express*, 2018, **5**, 045051.
21 L. Yang, X. Li, Z. Wang, Y. Shen and M. Liu, *Appl. Surf. Sci.*, 2017, **420**, 346–354.
22 Y. H. Zhang, Z. R. Tang, X. Z. Fu and Y. J. Xu, *Appl. Catal., B*, 2011, **106**, 445–452.
23 A. Kubacka, M. Fernandez-García and G. Colon, *Chem. Rev.*, 2012, **112**, 1555–1614.
24 A. M. Tripathi, R. G. Nair and S. K. Samdarshi, *Sol. Energy Mater. Sol. Cells*, 2010, **94**, 2379–2385.
25 D. W. Hwang, J. Kim, T. J. Park and J. S. Lee, *Catal. Lett.*, 2002, **80**, 53–57.
26 (*a*) S. Jianwen, *Chem. Eng. J.*, 2009, **151**, 241–246; (*b*) Q. Jiang, L. Wang, C. Yan, C. Liu, Z. Guo and N. Wang, *Eng. Sci.*, 2018, **1**, 64–68, DOI: 10.30919/es.180329; (*c*) H. L. Shindume, Z. Zhao, N. Wang, H. Liu, A. Umar, J. Zhang, T. Wu and Z. Guo, *J. Nanosci. Nanotechnol.*, DOI: 10.1166/jnn.2018.15745, in press.

 This journal is © The Royal Society of Chemistry 2018

Published on 25 June 2018. Downloaded by University of Tennessee at Knoxville on 9/5/2018 8:48:37 PM.

27 S. A. Rawool, M. R. Pai, A. M. Banerjee and A. Arya, *Appl. Catal., B*, 2018, **221**, 443–458.
28 S. Arias, Y. E. Licea, D. Soares, J. G. Eon and L. A. Palacio, *Catal. Today*, 2017, **296**, 187–196.
29 H. Ji, W. Wu, F. Li, X. Yu, J. Fu and L. Jia, *J. Hazard. Mater.*, 2017, **334**, 212–222.
30 J. Cai, Y. Zhang, B. Pan, W. Zhang, L. Lv and Q. Zhang, *Water Res.*, 2017, **102**, 109–116.
31 J. Das, B. S. Patra, N. Baliarsingh and K. M. Parida, *Appl. Clay Sci.*, 2006, **32**, 252–260.
32 Ci. Ezeh, M. Tomatis, X. Yang, J. He and C. Sun, *Ultrason. Sonochem.*, 2018, **40**, 341–352.
33 R. Li, R. Che, Q. Liu, S. Su, Z. Li, H. Zhang and J. Liu, *J. Hazard. Mater.*, 2017, **338**, 167–176.
34 L. Huang, S. Chu, J. Q. Wang, F. Kong, L. L. Luo, Y. Wang and Z. G. Zou, *Catal. Today*, 2013, **212**, 81–88.
35 S. J. Xia, F. X. Liu, Z. M. Ni, J. L. Xue and P. P. Qian, *J. Colloid Interface Sci.*, 2013, **405**, 195–200.
36 L. Zou, F. Li, X. Xiang, D. G. Evans and X. Duan, *Chem. Mater.*, 2006, **18**, 5852–5859.
37 G. Mendoza-Damián, F. Tzompantzi and A. Mantilla, *J. Hazard. Mater.*, 2013, **263**, 67–72.
38 G. Chen, S. Qian, X. Tu, X. Wei, J. Zou and L. Len, *Appl. Surf. Sci.*, 2014, **293**, 345–351.
39 G. Starukh, *Nanoscale Res. Lett.*, 2017, **12**, 391.
40 C. G. Silva, Y. Bouizi and V. Fornés, *J. Am. Chem. Soc.*, 2009, **131**, 13833–13839.
41 A. H. Iglesias, O. P. Ferreira, D. X. Gouveia, A. G. Souza Filho, J. A. C. de Paiva, J. M. Filho and O. L. Alves, *J. Solid State Chem.*, 2005, **178**, 142–152.
42 D. C. Carvalho, N. A. Ferreira, M. Josué Filho and O. P. Ferreira, *Catal. Today*, 2015, **250**, 155–165.
43 J. Li, W. Xu, R. Li, J. Luo, D. Zhou, S. Li and P. Cheng, *J. Mater. Sci.*, 2016, **51**, 9287–9295.
44 Y. N. Li, J. Su, X. Y. Lv, Y. F. Long and Y. X. Wen, *Electrochim. Acta*, 2015, **182**, 596–603.
45 S. A. Abdel Moaty, A. A. Farghali and M. Moussa, *J. Taiwan Inst. Chem. Eng.*, 2017, **71**, 441–453.
46 X. Xiang, L. Xie, Z. Li and F. Li, *Chem. Eng. J.*, 2013, **221**, 222–229.
47 W. Shi, F. Guo, C. Zhu, H. Wang, H. Li and H. Huang, *J. Mater. Chem. A*, 2017, **5**, 19800–19807.
48 C. Yang, G. Gao, Z. Guo, L. Song, J. Chi and S. Gan, *Appl. Surf. Sci.*, 2017, **400**, 365–374.
49 R. Benrabaa, A. Löfberg, A. Rubbens, E. Bordes-Richard, R. N. Vannier and A. Barama, *Catal. Today*, 2013, **203**, 188–195.
50 B. Q. Zhao, Q. Shao, L. Hao, L. Zhang, Z. Liu and B. Zhang, *J. Colloid Interface Sci.*, 2018, **511**, 39–47.
51 X. Cheng, X. Huang, X. Wang and D. Sun, *J. Hazard. Mater.*, 2010, **177**, 516–523.
52 R. K. Sahu, B. S. Mohanta and N. N. Das, *J. Phys. Chem. Solids*, 2013, **74**, 1263–1270.
53 X. R. Wang, P. X. Wu and Y. H. Lu, *Sep. Purif. Technol.*, 2014, **132**, 195–205.
54 A. A. A. Ahmed, Z. A. Talib and M. Z. bin. Hussein, *J. Solid State Chem.*, 2012, **191**, 271–278.
55 L. Q. Qwabe, H. B. Friedrich and S. Singh, *J. Mol. Catal. A: Chem.*, 2015, **404**, 167–177.
56 D. Pan, S. Ge, X. Zhang, X. Mai, S. Li and Z. Guo, *Dalton Trans.*, 2018, **47**, 708–715.
57 M. Li, X. Li, G. Jiang and G. He, *Ceram. Int.*, 2015, **41**, 5749–5757.
58 X. Li, L. Wang, L. Zhang and S. Zhuo, *Appl. Surf. Sci.*, 2015, **419**, 586–594.
59 D. Huang, J. Ma, C. Fan, K. Wang, W. Zhao, M. Peng and S. Komarneni, *Appl. Clay Sci.*, 2018, **152**, 230–238.
60 J. W. Tang, Z. G. Zou and J. H. Ye, *J. Phys. Chem. B*, 2003, **107**, 14265–14269.
61 M. Hussain, N. Russo and G. Saracco, *Chem. Eng. J.*, 2011, **166**, 138–149.
62 S. Adhikari and G. Madras, *Phys. Chem. Chem. Phys.*, 2017, **19**, 13895–13908.
63 L. Zhang, C. Dai, X. Zhang, Y. Liu and J. Yan, *Trans. Nonferrous Met. Soc. China*, 2016, **26**, 2380–2389.
64 P. R. Chowdhury and K. G. Bhattacharyya, *Photochem. Photobiol. Sci.*, 2017, **16**, 835–839.
65 F. Zhang, X. Li, Q. Zhao and A. Chen, *J. Phys. Chem. C*, 2016, **120**, 19113–19123.
66 M. Lan, G. Fan, W. Sun and F. Li, *Appl. Surf. Sci.*, 2013, **282**, 937–946.
67 Y. Lei, J. Huo and H. Liao, *RSC Adv.*, 2017, **7**, 40621–40631.
68 C. Han, Q. Shao, M. Liu, S. Ge, Q. Liu and J. Lei, *Mater. Sci. Semicond. Process.*, 2016, **56**, 166–173.
69 L. Wu, H. Yan, J. Xiao, X. Li, X. Wang and T. Zhao, *Ceram. Int.*, 2017, **16**, 14334–14339.
70 B. Song, T. Wang, H. Sun, Q. Shao, J. Zhao, K. Song, L. Hao, L. Wang and Z. Guo, *Dalton Trans.*, 2017, **46**, 15769–15777.
71 S. Chen, X. Yu, H. Zhang and W. Liu, *J. Hazard. Mater.*, 2010, **180**, 735–740.
72 X. Deng, H. Zhang, Q. Ma, Y. Cui, X. Cheng and X. Li, *Sep. Purif. Technol.*, 2017, **186**, 1–9.
73 J. Yan, S. Yang, Z. Xie, X. Li, W. Zhou and X. Zhang, *J. Solid State Electrochem.*, 2017, **21**, 455–461.
74 S. Li, S. Hu, K. Xu, W. Jiang, Y. Liu, Z. Leng and J. Liu, *J. Colloid Interface Sci.*, 2017, **504**, 561–569.
75 X. Xu, R. Lu, X. Zhao, S. Xu, X. Lei and F. Zhang, *Appl. Catal., B*, 2011, **102**, 147–156.
76 F. Dong, T. Xiong, S. Yan, H. Wang, Y. Sun and Y. Zhang, *J. Catal.*, 2016, **344**, 401–410.
77 M. Wu, C. Wang, Y. Zhao, L. Xiao, C. Zhang and X. Yu, *CrystEngComm*, 2015, **17**, 2336–2345.
78 (*a*) Q. Luo, H. Chen, Y. Lin, H. Du, Q. Hou, F. Hao, N. Wang, Z. Guo and J. Huang, *Adv. Funct. Mater.*, 2017, **27**, 1702090; (*b*) W. Hu, T. Liu, X. Yin, H. Liu, X. Zhao, S. Luo, Y. Guo, Z. Yao, J. Wang, N. Wang, H. Lin and Z. Guo, *J. Mater. Chem. A*, 2017, **5**, 1434–1441; (*c*) T. Liu, K. Yu, L. Gao, H. Chen, N. Wang, L. Hao, T. Li, H. He and Z. Guo, *J. Mater. Chem. A*, 2017, **5**, 17848–17855; (*d*) H. Chen,

Published on 25 June 2018. Downloaded by University of Tennessee at Knoxville on 9/5/2018 8:48:37 PM.

T. Liu, B. Wang, Z. Liu, Y. Li, Q. Zhao, N. Wang, H. He, H. Liu and Z. Guo, *Adv. Compos. Hybrid Mater.*, 2018, **1**, 356–363.

79 T. Su, Q. Shao, Z. Qin, Z. Guo and Z. Wu, *ACS Catal.*, 2018, **8**, 2253–2276.

80 (*a*) H. Gu, H. Zhang, J. Lin, Q. Shao, D. P. Young, L. Sun, T. D. Shen and Z. Guo, *Polymer*, 2018, **143**, 324–330; (*b*) H. Wei, H. Gu, J. Guo, D. Cui, X. Yan, J. Liu, D. Cao, X. Wang, S. Wei and Z. Guo, *Adv. Compos. Hybrid Mater.*, 2018, **1**, 127–134; (*c*) H. Wu, Y. Zhang, R. Yin, W. Zhao, X. Li and L. Qian, *Adv. Compos. Hybrid Mater.*, 2018, **1**, 168–176.

81 (*a*) B. Song, T. Wang, H. Sun, Q. Shao, J. Zhao, K. Song, L. Hao, L. Wang and Z. Guo, *Dalton Trans.*, 2017, **46**, 15769–15777; (*b*) Y. Zhang, L. Qian, W. Zhao, X. Li, X. Huang, X. Mai, Z. Wang, Q. Shao, X. Yan and Z. Guo, *J. Electrochem. Soc.*, 2018, **165**, H510–H516; (*c*) C. Lin, H. Hu, C. Cheng, K. Sun, X. Guo, Q. Shao, J. Li, N. Wang and Z. Guo, *Electrochim. Acta*, 2018, **260**, 65–72.

82 (*a*) Y. Feng, X. Jiang, E. Ghafari, B. Kucukgok, C. Zhang, I. Ferguson and N. Lu, *Adv. Compos. Hybrid Mater.*, 2018, **1**, 114–126; (*b*) Q. Luo, H. Ma, Q. Hou, *et al.*, *Adv. Funct. Mater.*, 2018, **28**, 1706777; (*c*) W. Deng, T. Kang, H. Liu, *et al.*, *Sci. Adv. Mater.*, 2018, **10**, 937–949.

This journal is © The Royal Society of Chemistry 2018